JCTC Journal of Chemical Theory and Computation

pubs.acs.org/JCTC Article

Trajectory Ensemble Methods Provide Single-Molecule Statistics for Quantum Dynamical Systems

Amro Dodin,[†] Justin Provazza,[†] David F. Coker,* and Adam P. Willard*

Cite This: *J. Chem. Theory Comput.* 2022, 18, 2047−2061 Read Online

ACCESS | Metrics & More | Article Recommendations

ABSTRACT: The emergence of experiments capable of probing quantum dynamics at the single-molecule level requires the development of new theoretical tools capable of simulating and analyzing these dynamics beyond an ensemble-averaged description. In this article, we present an efficient method for sampling and simulating the dynamics of the individual quantum systems that make up an ensemble and apply it to study the nonequilibrium dynamics of the ubiquitous spin-boson model. We generate an ensemble of single-system trajectories, and we analyze this trajectory ensemble using tools from classical statistical mechanics. Our results demonstrate that the dynamics of quantum coherence is highly heterogeneous at the single-system level due to variations in the initial bath configuration, which significantly affects the transient exchange of coherence between the system and its bath. We observe that single systems tend to retain coherence over time scales longer than that of the ensemble. We also compute a novel thermodynamic entanglement entropy that quantifies a thermodynamic driving force favoring system−bath entanglement.

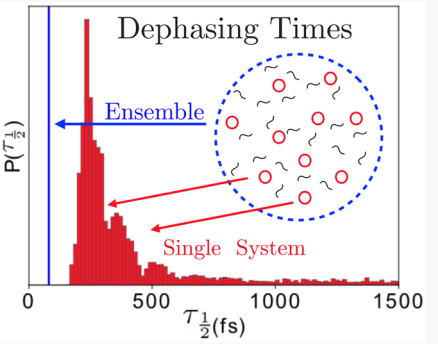

1. INTRODUCTION

Quantum mechanical systems, from quantum computers to photosynthetic light-harvesting complexes, display a great deal of variability between putatively identical systems. For example, uncontrolled variations in the environment and imperfections in device construction can lead to unpredictable behavior of individual systems and have the potential to limit the performance and reliability of quantum devices. Understanding the physical origins and effects of this heterogeneity can provide insight into the robustness and regulation of biomolecular processes and enable the design of more reliable quantum computing devices. However, observing and interpreting this dynamical variability require the development of new experimental techniques capable of measuring quantum systems at unprecedented spatiotemporal resolution and theoretical tools for efficiently sampling, simulating, and analyzing their dynamics. In this paper, we combine efficient quantum classical simulations with the recently developed state space formulation of quantum ensembles to investigate quantum dynamics at the single-molecule level. Our analysis shows how statistical mechanical tools inspired by classical molecular dynamics can be adapted to single-molecule quantum dynamics, providing new thermodynamic insight into quantum phenomena such as entanglement and coherence.

Single-molecule spectroscopies are broadly used to probe heterogeneous microscopic behavior in chemistry, physics, and biophysics.[1−3] These techniques have been successfully deployed to reveal single-molecule processes that cannot be seen at the ensemble level, including quantum dot blinking,[4] the hand-over-hand myosin motility mechanism,[5] and dissipative photoprotection in photosynthetic light harvesting.[6] While these techniques have found enormous success in probing classical processes, their reliance on slow, incoherent fluorescence complicates their use in the study of quantum systems. Instead, quantum dynamics is typically probed via coherent ultrafast spectroscopies[7] that use short broadband laser pulses to measure femtosecond dynamics, providing evidence for wavelike energy transport in photosynthesis[8−12] and coherent nuclear dynamics in retinal photosimerization—the first step in human vision.[13] However, the practical constraints of these spectroscopies require measurements on large ensembles of systems, preventing the study of heterogeneity in coherent dynamics.

In recent years, a new class of experiments has emerged that combines these spectroscopies to observe and control quantum dynamics at the single-molecule level.[14−17] These studies have revealed the heterogeneity of single-molecule behavior that underlies ensemble observations and showed that the dynamics of individual systems can be coherently

Received: May 13, 2021
Published: March 1, 2022

https://doi.org/10.1021/acs.jctc.1c00477
J. Chem. Theory Comput. 2022, 18, 2047−2061

controlled.[18] However, the microscopic complexity of the systems and their local nanoenvironments has prevented the experimental identification of the source of heterogeneity. Computational modeling of single-molecule dynamics can provide valuable insight into the microscopic degrees of freedom responsible for intersystem variability, enabling rationally designed single-molecule coherent and optomechanical control.

The dynamics of heterogeneous systems can be studied by analyzing the statistics of ensemble member dynamics, i.e., their trajectory ensembles. Such analysis has become common for systems that can be simulated with classical molecular dynamics. Numerous tools and theories, such as enhanced sampling methods[19,20] and fluctuation theorems,[21−25] have been developed to enable the analysis and interpretation of trajectory ensemble data. Extending these methods to quantum systems can be problematic due to uncertainty in system trajectories within classical phase space. However, we have recently shown that these problems can be eliminated by resolving trajectories in the state space of density operators.[26] We utilize this state space approach here to enable the analysis of a quantum trajectory ensemble.

Intuitively, the trajectory ensemble can be understood in analogy with the simulation of classical systems by molecular dynamics as follows. First, an ensemble of initial system−bath states is sampled from an appropriate distribution. Then, the total system−bath quantum dynamics for each initial state is evolved forward in time in analogy to the constant energy propagation of classical molecular dynamics. The total system−bath dynamics of each ensemble member can then be projected onto the system subspace through a partial trace over the bath degrees of freedom, leading to a system state that is a collective coordinate of the total system−bath description. This leads to an ensemble of system state trajectories equivalent to molecular dynamics trajectories of classical collective coordinates (e.g., order parameters).

The primary challenge in extending this molecular dynamics paradigm to quantum systems is the identification of an appropriate initial state distribution. The assertion that a collection of quantum systems probed in an experiment displays some heterogeneity is, in itself, not surprising. For instance, one would certainly expect that the protein scaffolds in a collection of photosynthetic light-harvesting complexes will undergo conformational fluctuations that can alter the configurations of charged side chains, the local solvation structure, or even the spatial arrangement of chromophores and therefore the dynamics of excitation energy transport through the chromophore network. Indeed, this heterogeneity in photosynthetic energy transport has been experimentally observed through ultrafast single-molecule spectroscopy.[15] The question, then, is how to identify and represent the initial system−bath states in a given physical context. Below, we will discuss several different methods for obtaining such an initial distribution, when each approach is applicable, and consequently how we can interpret the resulting trajectory ensemble.

As a concrete example, we consider coherent excitation energy transfer upon the impulsive excitation of an ensemble of chromophore pairs embedded in a condensed phase environment. The electronic excitation is the quantum *system* that we are interested in analyzing. This electronic system is coupled to a *bath* of nuclear modes (e.g., intramolecular vibrations) with which it can form entanglement and transfer energy thereby modifying the coherent energy transfer dynamics. This bath of nuclear degrees of freedom is itself weakly coupled to a larger condensed phase *environment* that acts as an energy source and sink thermalizing the bath. As is usually done in condensed phase quantum dynamics simulations, the system is defined as the degrees of freedom over which the observables of interest are defined. We include all degrees of freedom that impact energy transfer dynamics on the time scale of interest in the bath. The remaining degrees of freedom which negligibly impact system−bath dynamics on this time scale are included in the environment. Using this convention, the only role played by the environment is thermalizing the initial state of the bath, and it is otherwise neglected in our analysis.

In this case, the initial system state is determined by the impulsive excitation assumption with all systems in the ensemble initialized with the excitation localized on the donor state. The bath of nuclear vibrations is initially thermalized in the ground state due to weak interactions with the environment over a long time before excitation. We then consider the initial state of each ensemble member's bath to be described by a product of localized minimum uncertainty coherent states whose centers are sampled from an appropriate distribution such that the ensemble reproduces the ground state thermal distribution. Below, we discuss how this initial state distribution is operationally well-defined as the limiting case of what can be observed in an idealized single-molecule experiment, commenting on how to apply this to realistic experiments with specified spatiotemporal resolution. We will also discuss how this initial distribution can be reached from our knowledge that heavier nuclear degrees of freedom tend to behave classically as localized particles and how this intuition can be rigorously applied and extended through pointer state analysis.

The article is outlined as follows: In Section 2, we present the *P*-ensemble description of the density matrix as an unraveling of the standard ensemble description and discuss important equilibrium and dynamical properties of systems described within the *P*-ensemble framework. In Section 3, we present a simple spin-boson model as a representation of a condensed phase molecular donor−acceptor pair. We describe the decomposition of an equilibrium Boltzmann distribution (describing the initial state of the bosonic bath) as a product of minimum uncertainty coherent states whose centers are distributed according to an effective-temperature Boltzmann distribution, for which we provide multiple justifications, and outline our numerical implementation of the single-system density matrix dynamics. In Section 4, we present results highlighting heterogeneity within the dynamics of single-system density matrices and contrast them with the ensemble density matrix description. Finally, we make concluding remarks and highlight potential applications of this theory in Section 5.

2. THEORETICAL FORMALISM

In this section, we present a formalism for analyzing the statistical distribution of single quantum system dynamics from within an ensemble. This formalism explicitly resolves the evolution of individual systems in a quantum state space that naturally lends itself to interpretation through the intuitive framework of classical statistical mechanics. We contrast this formalism with the traditional density matrix formalism used for describing quantum ensembles.

https://doi.org/10.1021/acs.jctc.1c00477
J. Chem. Theory Comput. 2022, 18, 2047−2061

The utility of our choice of formalism can be illustrated by considering two different hypothetical experiments. In the first experiment, a large number of sample systems are simultaneously excited by a laser pump sequence and then allowed to evolve for some time τ, after which a probe sequence is applied to measure their state. In the second experiment, the same sample is diluted such that only a single quantum system resides within the path of the pump and probe lasers, thus allowing for repeated initialization and measurement of single systems. Unlike the first experiment, which reports on the average properties of an ensemble, the second experiment can provide explicit information about the distribution of states and its dynamics. The theoretical basis for studies in nonequilibrium dynamics relies on the knowledge of this distribution and its temporal evolution.

2.1. Quantum Ensembles and Observables. The outcome of ensemble experiments is completely described within the ensemble density matrix, ρ. The expectation value of any observable A that can be measured in such an experiment can be computed directly from this density matrix as

$$\bar{A}[\rho] = \mathrm{Tr}\{A\rho\} \tag{1}$$

The ρ-ensemble is widely used to describe quantum systems embedded in an environment. As such, a large number of theoretical and computational tools have been developed to characterize the dynamics and statistical mechanical properties of ρ.[27,28] However, despite encoding information about the statistics of observed properties, the ensemble density matrix, ρ, does not contain the necessary information to discern the statistics of individual systems or their heterogeneity.

This single-system information is contained within our quantum state space formalism. Specifically, the properties of each individual system are described by a single-system density matrix, Γ, that captures its intrinsic quantum uncertainties. The overall state of the ensemble is then given by a probability distribution, $P(\Gamma)$, which specifies the fraction of single systems that are in a given state. This construction separately treats quantum uncertainty, as encoded by Γ, and the classical heterogeneity through the distribution $P(\Gamma)$. By definition, the properties of density matrices are retained by Γ, and the distribution $P(\Gamma)$ behaves in Liouville space analogously to a classical ensemble distribution on position−momentum phase space.[26]

A description of an ensemble system by ρ is hereby referred to as a ρ-ensemble representation, while a description incorporating $P(\Gamma)$ is referred to as a P-ensemble representation. The P-ensemble contains more information than its corresponding ρ-ensemble. A ρ-ensemble can be recovered from the P-ensemble through a simple averaging, via

$$\rho = \langle\Gamma\rangle = \int \mathrm{d}\Gamma\Gamma P(\Gamma) \tag{2}$$

where $\langle\cdot\rangle$ represents the average over the distribution $P(\Gamma)$, and the integral is taken over the set of all density matrices. However, a P-ensemble cannot be unambiguously specified from a given ρ.

The P-ensemble was first proposed by Davies in the mathematical study of quantum stochastic processes[28,29] and has been applied in the formulation of stochastic unraveling methods for quantum dynamics simulations[30−33] and in the theory of closed loop quantum feedback control.[34,35] In these previous contexts, the distribution was used to describe a Monte Carlo process introduced for numerical convenience or was generated by the repeated collapse of the quantum state due to continuous measurement.[36,37] We apply a similar mathematical framework here to describe a distribution that arises due to heterogeneity between quantum systems (see ref 26 for a detailed discussion of the relationship between these different distributions and the physical situations that they describe). In all of these applications, the P-ensemble must be introduced since the ensemble average that defines ρ in eq 2 integrates out important information.

The P-ensemble is able to characterize certain observables reporting on the heterogeneity between members of an ensemble that are not possible to formulate in the ρ-ensemble. A simple example of this is the variance of an observable A. In the ρ-ensemble, only one variance can be defined:

$$\mathrm{Var}_\rho[A] = \overline{A^2}[\rho] - \bar{A}[\rho]^2 = \mathrm{Tr}\{A^2\rho\} - \mathrm{Tr}\{A\rho\}^2 \tag{3}$$

where the average defined by the overbar is that of eq 1. This expression corresponds to the overall variations of the observable A. In the P-ensemble, however, this variance can be split into two, separately observable, contributions. Using eq 2, the ρ-ensemble variance can be decomposed as

$$\begin{aligned}\mathrm{Var}_\rho[A] &= \langle \mathrm{Var}_\Gamma[A]\rangle + \mathrm{Var}_P[\bar{A}] \\ &= \int \mathrm{Tr}\{A^2\Gamma\}P(\Gamma)\mathrm{d}\Gamma - \left(\int \mathrm{Tr}\{A\Gamma\}P(\Gamma)\mathrm{d}\Gamma\right)^2\end{aligned} \tag{4a}$$

$$\begin{aligned}\langle \mathrm{Var}_\Gamma[A]\rangle &= \langle \mathrm{Tr}\{A^2\Gamma\} - \mathrm{Tr}\{A\Gamma\}^2\rangle \\ &= \int \mathrm{Tr}\{A^2\Gamma\}P(\Gamma)\mathrm{d}\Gamma - \int \mathrm{Tr}\{A\Gamma\}^2P(\Gamma)\mathrm{d}\Gamma\end{aligned} \tag{4b}$$

$$\begin{aligned}\mathrm{Var}_P[\bar{A}[\Gamma]] &= \langle \bar{A}^2[\Gamma]\rangle - \langle \bar{A}[\Gamma]\rangle^2 \\ &= \int \mathrm{Tr}\{A\Gamma\}^2P(\Gamma)\mathrm{d}\Gamma \\ &\quad - \left(\int \mathrm{Tr}\{A\Gamma\}P(\Gamma)\mathrm{d}\Gamma\right)^2\end{aligned} \tag{4c}$$

where $\mathrm{Var}_P[\bar{A}[\Gamma]]$ captures differences in the average values of A across different systems in the ensemble and $\langle \mathrm{Var}_\Gamma[A]\rangle$ captures how much of the variance comes from uncertainty in the outcome of A at the single-system level. This equality can be seen by adding and subtracting the term $\int \mathrm{Tr}\{A\Gamma\}^2P(\Gamma)\mathrm{d}\Gamma$ in eq 4a and splitting the resulting four terms into eqs 4b and 4c. These two observables highlight the ability of P-ensemble descriptions, and the single-molecule experiments that they model, to capture heterogeneity within an ensemble of individually addressable systems.

2.2. Thermodynamic Equilibrium. Systems described by the quantum P-ensemble are subject to a Boltzmann-like probability distribution law. The derivation of this distribution follows that for purely classical ensembles, i.e., maximizing distributional entropy subject to a constraint on the ensemble average energy.[38−40] In the P-ensemble, we maximize $S = \int P(\Gamma)\ln(P(\Gamma))\mathrm{d}\Gamma$, subject to a constraint that the ensemble density matrix satisfies the Gibbs state:

$$\rho = \langle\Gamma\rangle = \frac{\mathrm{e}^{-\beta H}}{\mathrm{Tr}\{\mathrm{e}^{-\beta H}\}} \tag{5}$$

where $\beta = \frac{1}{k_B T}$ and H is the Hamiltonian. For an N-dimensional system, the Gibbs state imposes N constraints

https://doi.org/10.1021/acs.jctc.1c00477
J. Chem. Theory Comput. 2022, 18, 2047−2061

on the diagonal components of the density matrix and $N(N-1)/2$ constraints on the off-diagonal matrix elements. Incidentally, the Gibbs constraint is significantly more complicated than simply fixing the mean energy, as is used to define the classical canonical distribution. Nevertheless, this constraint yields a Boltzmann-like distribution over the set of density matrices:

$$P(\Gamma) = \frac{e^{-\beta \bar{H}[\Gamma]}}{Y} \tag{6}$$

where $\bar{H}[\Gamma] = \mathrm{Tr}\{H\Gamma\}$ is the quantum average over state Γ, and $Y = \int d\Gamma e^{-\beta \bar{H}[\Gamma]}$ is the state space partition function.

For composite systems comprised of a system with Hilbert space $\mathcal{H}_S$ and a bath with Hilbert space $\mathcal{H}_B$, the density matrix, Γ, is an operator acting on the tensor product space $\mathcal{H}_S \otimes \mathcal{H}_B$. In this case, the reduced system density matrix $\sigma = \mathrm{Tr}_B\Gamma$ can be understood as a lower dimensional collective coordinate of the total density matrix Γ. We define a constrained energy, entropy, and free energy for each state σ in the same manner as a classical collective coordinate

$$\begin{aligned} F[\sigma] &\equiv -k_B T \ln\left(\int \delta(\sigma - \mathrm{Tr}_B\Gamma) e^{-\beta \bar{H}[\Gamma]} d\Gamma\right) \\ &= H_{MF}[\sigma] - TS_e[\sigma] \end{aligned} \tag{7}$$

where

$$H_{MF}[\sigma] = \int \bar{H}[\Gamma] \delta(\sigma - \mathrm{Tr}_B\Gamma) e^{-\beta(\bar{H}[\Gamma] - F[\sigma])} d\Gamma \tag{8}$$

is the reduced system Hamiltonian of mean force. If the Hamiltonian $H = H_S + H_B + V$ can be split into system, H_S, bath, H_B, and coupling V Hamiltonians, then the distribution in eq 6 can be projected onto the space of system (reduced) density matrices using the projection $\Gamma \to \sigma = \mathrm{Tr}_B\Gamma$. In the large bath (or equivalently weak coupling) limit $|V| \ll |H_B|$, and thus $H_{MF}[\sigma] \approx \bar{H}_s[\sigma]$,[41] giving

$$P(\sigma) = \frac{e^{-\beta(\bar{H}_S[\sigma] - TS_e[\sigma])}}{Z} \tag{9}$$

where $Z = \int d\sigma e^{-\beta(\bar{H}_S[\sigma] - TS_e[\sigma])}$ is the state space partition function, and $S_e[\sigma] \equiv k_B \int d\Gamma \delta(\sigma - \mathrm{Tr}_B\Gamma) e^{-\beta(\bar{H}_B[\Gamma] + \bar{V}[\Gamma])}$ is the entropy associated with the system−bath entanglement.

2.3. State Space Geometry and Dynamics. The population dynamics of a quantum P-ensemble can be characterized by a quantum Liouville theorem for P-ensembles. This theorem can be derived by first considering the equations of motion for individual ensemble members, as given by the Liouville−von Neumann equation for the total system−bath evolution. In the state space of density operators, these equations of motion take a fluid dynamical form where the probability density flows along a vector field defined by the time derivative of the density matrices at each point in the state space.[26]

The directionality of flow on this state space is defined by the trace inner product on the Liouville space of operators. This dot product of two operators, A and B, is thus defined as

$$A \cdot B = \mathrm{Tr}\{A^\dagger B\} \tag{10}$$

For any given basis of the system Hilbert space $\{e_i\}$ a standard orthonormal basis can be constructed for the Liouville space $\{E_{ij} = |e_i\rangle\langle e_j|\}$ such that the trace inner product defines the operator matrix elements $A_{ij} = A \cdot E_{ij}$.

We have previously shown that under the Liouville−von Neumann equation for closed system evolution, the probability distribution takes the incompressible convective form

$$\frac{\partial}{\partial t} P(\Gamma, t) = -\nabla_\Gamma P(\Gamma, t) \cdot \dot{\Gamma} \tag{11}$$

where ∇_Γ denotes the gradient on Liouville space and $i\hbar\dot{\Gamma} = [H, \Gamma]$ is the dynamical evolution vector field defined by the Liouville−von Neumann equation. This approach can be generalized to open systems using the Nakajima−Zwanzig equation for system dynamics,[26] where interaction with the bath introduces dissipative frictional contributions that drive the narrowing of the distribution to a single point and stochastic bath kicks that lead to the broadening of the distribution. The thermal steady state given by eq 9 reflects a balance of these two opposing bath contributions implying a fluctuation−dissipation relation.

Due to its similarity to classical dynamics, the P-ensemble Liouville theorem enables an intuitive analysis and interpretation of single-system quantum dynamics. Using a trajectory ensemble approach, a set of initial conditions can be sampled from an initial state space distribution $P(\Gamma, 0)$ and then propagated in time to produce an ensemble of trajectories. This trajectory ensemble can then be analyzed to determine the time-dependent state distribution. Such an approach is similar to classical molecular dynamics simulations and allows any method for propagating the underlying equations of motion to be used to compute the distribution dynamics. Moreover, the statistics of system dynamics can be computed directly from the trajectory ensemble with each member of the ensemble representing the dynamics of a single molecule within the ensemble. In the remainder of this paper, we will describe the implementation of such a trajectory ensemble approach in the setting of the standard spin-boson model to illustrate how thermodynamic insight can be gained in single-molecule quantum dynamics.

3. NUMERICAL METHODS: SPIN-BOSON MODEL

For proof-of-concept numerical simulations, we utilize the uncorrelated bath spin-boson model that consists of two discrete "spin" states, each of which is coupled bilinearly to a set of harmonic oscillators. Such a model is often utilized as a simple representation of a molecular donor−acceptor pair in the condensed phase, where the two spin states represent localized electronic excitations on the donor and acceptor molecules and the independent baths represent the local vibrational normal modes coupled to these excitations (e.g., the intramolecular vibrations of the donor and acceptor). In the Meyer−Miller−Stock−Thoss (MMST) mapping representation,[42−44] obtained by replacing the quantum system state projection operators with bosonic raising and lowering operators as $|\alpha\rangle \to \hat{a}_\alpha^\dagger$, the Hamiltonian can be expressed as

$$\begin{aligned} \hat{H} &= \frac{1}{2} \sum_{\alpha \in (0,1)} \sum_{k_\alpha=1}^{D} (\hat{P}_{k_\alpha}^2 + \omega_{k_\alpha}^2 \hat{R}_{k_\alpha}^2) + \sum_{\alpha,\beta \in (0,1)} h_{\alpha\beta}(\hat{\mathbf{R}}) \hat{a}_\alpha^\dagger \hat{a}_\beta \\ &= \frac{1}{2} \sum_{\alpha \in (0,1)} \sum_{k_\alpha=1}^{D} (\hat{P}_{k_\alpha}^2 + \omega_{k_\alpha}^2 \hat{R}_{k_\alpha}^2) + \frac{1}{2\hbar} \sum_{\alpha,\beta \in (0,1)} h_{\alpha\beta}(\hat{\mathbf{R}}) \\ &\quad \times (\hat{q}_\alpha \hat{q}_\beta + \hat{p}_\alpha \hat{p}_\beta - \hbar\delta_{\alpha\beta}) \end{aligned} \tag{12}$$

https://doi.org/10.1021/acs.jctc.1c00477
J. Chem. Theory Comput. 2022, 18, 2047−2061

where $h_{\alpha\beta}(\hat{\mathbf{R}}) = \left(\epsilon_\alpha + \sum_{k_\alpha=1}^{D} c_{k_\alpha}^{\alpha}\hat{R}_{k_\alpha}\right)\delta_{\alpha\beta} + \Delta_{\alpha\beta}(1-\delta_{\alpha\beta})$ describes the coupling between each of the spin states and their independent baths, as well as the coupling between the spin-up $|1\rangle$ and spin-down $|0\rangle$ states. Here, we have chosen $\epsilon_0 - \epsilon_1 = \Delta_{01} = 100\ \mathrm{cm}^{-1}$.

Each state's independent (but identical) bath is characterized by the spectral density defined, in this case, by the Drude−Lorentz form as

$$J(\omega) = 2\lambda\frac{\omega\gamma}{\omega^2+\gamma^2} = \frac{\pi}{2}\sum_{k=1}^{D}\frac{c_k^2}{\omega_k}\delta(\omega-\omega_k) \tag{13}$$

with bath correlation time $\gamma^{-1} = 50$ fs and reorganization energy $\lambda = 20\ \mathrm{cm}^{-1}$. These values are typical for describing the impact of solvent fluctuations on the electronic excitation of molecular chromophore systems in solution. We have represented the spectral density by sampling $D = 200$ modes from each of the independent baths according to the methodology described in ref 45.

3.1. Quantum Dynamics Algorithm. Computing the time evolution of high-dimensional quantum systems relies on approximations or assumptions to circumvent the issue of an exponentially scaling state space. To demonstrate the theoretical framework alluded to above, we apply the partially linearized density matrix (PLDM) dynamics algorithm,[46] a mixed quantum classical propagation scheme that treats the relevant degrees of freedom quantum mechanically and the irrelevant degrees of freedom explicitly in a classical-like manner. Crucially, the PLDM algorithm makes no inherent assumption about the initial state of the system, allowing one to deconvolute the dynamics of, in our application here, a thermal distribution of states into a heterogeneous ensemble of single-molecule realizations. This, in turn, provides access to the underlying statistical properties of a heterogeneous dynamical ensemble of single-molecule systems.

The PLDM algorithm, which combines a semiclassical coherent state path integral description of the quantum subsystem within the MMST mapping representation with a truncated Wigner approximation for the dynamics of the bath,[47] has proven fruitful in describing nonequlibirum dynamics of open quantum systems.[48−52] Since a semiclassical dynamical description of the mapping variables (as defined by the Hamiltonian in eq 12) is quantum mechanically exact, the central approximations of the PLDM algorithm are the linearization of the bath phase space path integrals (the so-called truncated Wigner approximation) and the neglect of the quantum subsystem's parametric dependence on quantum fluctuations about the bath's linearized (classical) trajectory.[46,48,50] A detailed description of the PLDM derivation has been presented previously, so we refer the interested reader to this literature[46,48] for such details and simply present the final result for an approximate time-evolved reduced density matrix element as

$$\begin{aligned}\sigma_{n_t,n_t'}(t) \approx \frac{1}{4\hbar^2}\int d\mathbf{R}_0\frac{d\mathbf{P}_0}{(2\pi\hbar)^{2D}}\sum_{n_0,n_0'=1}^{N_s} W^{(n_0,n_0')}(\mathbf{P}_0,\mathbf{R}_0)\\ \times\int\frac{d\mathbf{q}_0 d\mathbf{p}_0}{(2\pi\hbar)^{N_s}}\frac{d\mathbf{q}_0' d\mathbf{p}_0'}{(2\pi\hbar)^{N_s}}\\ \times\mathcal{G}(\mathbf{q}_0,\mathbf{p}_0)\mathcal{G}(\mathbf{q}_0',\mathbf{p}_0')(q_t^{(n_t)}+ip_t^{(n_t)})(q_0^{(n_0)}-ip_0^{(n_0)})\\ \times(q_0'^{(n_0')}+ip_0'^{(n_0')})(q_t'^{(n_t')}-ip_t'^{(n_t')})\end{aligned} \tag{14}$$

Here $W^{(n_0,n_0')}(\mathbf{P}_0,\mathbf{R}_0)$ is the partial Wigner transform with respect to the bath degrees of freedom of the (n_0, n_0')-th system matrix element of the initial density operator, $\mathcal{G}(\mathbf{q}_0,\mathbf{p}_0) = \exp\left[-\frac{1}{2}\sum_{\alpha=1}^{N_s}(q_0^{(\alpha)2}+p_0^{(\alpha)2})\right]$ provides a Gaussian distribution of mapping variable initial conditions, and mapping variables with a subscript t are obtained by propagating classical trajectories from their initial conditions (labeled with a subscript 0).

The PLDM algorithm is numerically implemented by performing integrals over initial conditions through a Monte Carlo sampling procedure to generate an ensemble of independent initial conditions in phase space, integrating Hamilton's equations of the form

$$\begin{aligned}\dot{R}_\tau &= \mathbf{M}^{-1}\cdot\mathbf{P}_\tau\\ \dot{P}_\tau &= -\nabla_{\mathbf{R}_\tau}V_0(\mathbf{R}_\tau) - \frac{1}{2}\nabla_{\mathbf{R}_\tau}(\tilde{h}_m(\mathbf{p}_\tau,\mathbf{q}_\tau,\mathbf{R}_\tau)\\ &\quad + \tilde{h}_m(p'_\tau,q'_\tau,\mathbf{R}_\tau))\\ \dot{q}_\tau^{(\alpha)} &= \frac{\partial\tilde{h}_m(\mathbf{p}_\tau,\mathbf{q}_\tau,\mathbf{R}_\tau)}{\partial p_\tau^{(\alpha)}} = \frac{1}{\hbar}\sum_{\beta=1}^{N_s}h_{\alpha\beta}(\mathbf{R}_\tau)p_\tau^{(\beta)}\\ \dot{p}_\tau^{(\alpha)} &= -\frac{\partial\tilde{h}_m(\mathbf{p}_\tau,\mathbf{q}_\tau,\mathbf{R}_\tau)}{\partial q_\tau^{(\alpha)}} = -\frac{1}{\hbar}\sum_{\beta=1}^{N_s}h_{\alpha\beta}(\mathbf{R}_\tau)q_\tau^{(\beta)}\end{aligned} \tag{15}$$

and computing each trajectory's contribution to the time-evolved density matrix elements according to the Hermite polynomial terms in eq 14. In the above expressions, $V_0(\mathbf{R})$ incorporates a state independent, bare bath potential, and $\tilde{h}_m(\mathbf{p}_\tau,\mathbf{q}_\tau,\mathbf{R}_\tau)$ is the second term in eq 12 after dropping the Kronecker delta that arises from mapping variable canonical commutation relations.[53]

Duplicate mapping variable equations of motion of the form given in the last two lines of eq 15 must be propagated for the unprimed ("forward") and primed ("backward") mapping variables. These different mapping variable initial conditions are propagated independently for the forward and backward mapping variables using the Hamiltonian defined by the same mean nuclear path $\mathbf{R}_\tau$.

For the spin-boson model parametrized as described above, which is characterized by relatively weak system−bath interactions, the PLDM algorithm has been shown to reproduce exact results nearly quantitatively for the ensemble description.[54] In support of these findings, it has recently been shown that the leading order quantum correction to PLDM is quadratic in the system−bath coupling strength.[54] As such, while approximate, we expect that this dynamics scheme will provide a reasonable description of the decoherence and entanglement time scales underlying the single-molecule density matrix dynamics considered here.

https://doi.org/10.1021/acs.jctc.1c00477
J. Chem. Theory Comput. 2022, 18, 2047−2061

3.2. Sampling Single-Molecule Bath Configurations.

The initial density operator is chosen in factorized form as

$$\hat{\rho}_0 = \hat{\rho}^S \otimes \hat{\rho}^B = |0\rangle\langle 0| \otimes \frac{e^{-\beta \hat{H}_B}}{Z_B} \tag{16}$$

where $\hat{H}_B = \frac{1}{2}\sum_{\alpha\in(0,1)}\sum_{k_\alpha=1}^{D}(\hat{P}_{k_\alpha}^2 + \omega_{k_\alpha}^2 \hat{R}_{k_\alpha}^2)$ is the bare bath Hamiltonian. Wigner transformation of the initial bath density operator yields the bath Wigner function as

$$W(\boldsymbol{R}, \boldsymbol{P}) \propto \prod_k \exp\left[-\left(\frac{P_k^2}{2\sigma_{P_k}^2} + \frac{R_k^2}{2\sigma_{R_k}^2}\right)\right] \tag{17}$$

with $\sigma_{P_k} = \sqrt{\frac{\hbar\omega_k}{2\tanh[\beta\hbar\omega_k/2]}}$ and $\sigma_{R_k} = \sqrt{\frac{\hbar}{2\omega_k \tanh[\beta\hbar\omega_k/2]}}$ defining the quantum distributions of bath momenta and positions, respectively.

The position and momentum component Gaussian distributions of the bath's thermal Wigner function can each be expressed as a convolution of, for example, two auxiliary Gaussian functions with widths $\sigma_{P_k}^{(1)}$ and $\sigma_{P_k}^{(2)}$ provided that these auxiliary distribution widths satisfy $\sigma_{P_k}^{(1)2} + \sigma_{P_k}^{(2)2} = \sigma_{P_k}^2$, with analogous definitions for the position distribution widths. Utilizing this convolution property, the initial bath configurations that give rise to a heterogeneous ensemble of Liouville space trajectories are chosen by sampling the centers of minimum uncertainty coherent states for each mode from an effective-temperature Boltzmann distribution since the Wigner function can be expressed as

$$W(\boldsymbol{R}, \boldsymbol{P}) \propto \int d\boldsymbol{P}' d\boldsymbol{R}' e^{-\sum_k \beta_k'(\frac{1}{2}P_k'^2 + \frac{1}{2}\omega_k^2 R_k'^2)} e^{-\sum_k \frac{(P_k - P_k')^2}{\hbar\omega_k}} \times e^{-\sum_k \frac{\omega_k (R_k - R_k')^2}{\hbar}} \tag{18}$$

where $\beta_k' = \frac{1}{k_B T_k'}$, with $T_k' = \frac{1}{k_B}\frac{\hbar\omega_k}{2}\left[\frac{1}{\tanh\left(\frac{\beta\hbar\omega_k}{2}\right)} - 1\right]$. The Wigner transforms of these coherent states have the form

$$g_{W_k'}(R_k, P_k) \propto e^{-(P_k - P_k')^2/\hbar\omega_k} e^{-\omega_k (R_k - R_k')^2/\hbar} \tag{19}$$

for the kth mode. It can readily be shown that this choice of bath density decomposition is equivalent to choosing the single-system density operator as a product of coherent state projection operators, $\hat{\Gamma} = \prod_k |R_k', P_k'\rangle\langle R_k', P_k'|$, with coherent state width parameters chosen so that

$$\langle x_k | R_k', P_k' \rangle = \left(\frac{\omega_k}{\pi\hbar}\right)^{1/4} e^{-\omega_k/2\hbar(x_k - R_k')^2 + i/\hbar P_k'(x_k - R_k')} \tag{20}$$

We then find that the distribution function of single-system density operators that satisfies eq 2, $P(\hat{\Gamma})$ (given our choice of ensemble bath density operator), is provided by the effective-temperature Boltzmann distribution in eq 18.

This statistical decomposition scheme of the thermal density operator into minimum uncertainty wavepackets is not mathematically unique. In fact, there exist an infinite number of different decomposition schemes (i.e., $P(\Gamma)$) that reproduce the same initial density operator. This reflects the increased information content of a P-ensemble description of an ensemble compared to the ρ-ensemble description, as represented in eq 2. Correspondingly, selecting this particular decomposition scheme reflects an input of additional information regarding the experimental scenario being considered.

We can reach this minimum uncertainty coherent state decomposition in several physically important ways. While these justifications are related, and all valid, they lead to slightly different interpretations of what the trajectory ensemble is representing. (More precisely, they determine the ontological and epistemic status of the trajectory ensemble. That is, they determine whether the trajectory ensemble represents a state of knowledge about a collection of systems or the physical quantum states of those systems.) Naïvely, one could simply insert this decomposition as an axiomatic assumption. In this case, the trajectory ensemble is simply an information theoretical object that propagates (under the action of physical laws) the information that we introduce with that assumption. The utility and ultimate physical reality of this trajectory ensemble are then determined by the utility or physical reality of the axiomatic assumption which is considered separately from the ensemble itself. In the absence of any further physical justification, this particular coherent state decomposition corresponds to the assumption that we have obtained the maximum possible information about the initial configuration of the bath that is allowed by quantum mechanics. It is therefore useful, as a limiting case of what is knowable about the system in contact with a bosonic bath.

Concretely, we reach this decomposition by considering an experiment where we measure the (Heisenberg-limited) initial positions and momenta of all bath oscillators the instant before exciting the donor dye molecule. In this case, each trajectory is a complete description of the observables of the excitonic system *conditioned* on the results of the bath measurements. That is, the trajectory ensemble represents the predicted outcome of a specific experiment. This experiment physically realizes the situation assumed above where the maximum bath information is acquired. One is free to consider other experimental conditions where different bath conditioning schemes are employed by decomposing the system into the *a posteriori* states of that scheme.[37] For example, if we consider a system where only some subset of the bath modes is measured (e.g., the slow modes of the bath), then we can decompose only those modes using the coherent state scheme and average over the full thermal distribution of the other modes. This approach simply employs the usual ρ-ensemble averaging procedure over the unobserved modes while decomposing the observed ones. We note that such an experiment does not necessarily require that the bath is explicitly measured and the outcome recorded. All that is needed is that we can guarantee that a collection of measurements corresponds to the same bath state. In single-molecule experiments, this arises when some subset of bath modes is slow compared to the measurement time of the experiment. Repeated measurements in a single molecule are therefore taken at a fixed value of that bath mode.

Finally, this minimum uncertainty decomposition can be reached without reference to any particular experimental measurement of the bath by considering the preferred (pointer state) basis of a system in a condensed phase environment. We assume that the total spin-boson composite is weakly coupled to a superenvironment of ambient particles such as solvent molecules or even ambient photons. Before the donor is excited, these particles will continuously scatter off the nuclei described by the boson bath. This ongoing scattering process

https://doi.org/10.1021/acs.jctc.1c00477
J. Chem. Theory Comput. 2022, 18, 2047−2061

acts as a measurement (in the von Neumann sense) of the boson bath since the angle and momentum of the ambient particles after the scattering event depend on the positions and momenta of the bosonic modes. This leads to environment-induced superselection (sometimes abbreviated as einselection) into a preferred basis of minimum uncertainty coherent states.[55−57] The minimum uncertainty decomposition scheme is therefore *the* unique scheme imposed by the preferred basis resulting from an environment of scattering particles. Intuitively, the environment of scattering particles encodes "which path" information about the position and momentum of each mode that is equivalent to performing a Heisenberg-limited measurement of their configuration as we described above. This decomposition into minimum uncertainty wavepackets can in fact be derived *ab initio* by explicitly considering the dynamics of the bosonic bath (before donor excitation) in contact with a scattering environment.[55,57] In this case, the trajectory ensemble is an objective (and dynamically verifiable) representation of the state of the spin-boson model under the action of a scattering bath performing which-path measurements. (As a subtlety, we note that we have assumed that the coupling to the environment is sufficiently weak that it does not affect the system−bath dynamics on the time scales considered. This corresponds to an assumption that the ambient particles are dilute.) This approach can be generalized to other types of environments (e.g., isolated high-quality optical cavities) by decomposing into their pointer state basis.[56,58]

These decomposition schemes allow us to unambiguously define a *P*-ensemble representation for a broad range of systems. The information theoretical decomposition scheme is simply a formal prescription for how external information can be encoded into the *P*-ensemble and is therefore applicable whenever such information is provided. We can apply the measurement-induced decomposition scheme whenever we are provided with a collection of (potentially weak) bath measurements upon which we can condition. In practice, this requires the construction of a realistic model of the bath degrees of freedom that are conditioned upon, which may not always be available.

The pointer state decomposition scheme is particularly useful since it can be defined directly from a Hamiltonian expressed as a sum $\hat{H} = \hat{H}_S + \hat{H}_B + \hat{H}_E + \hat{V}_{SB} + \hat{V}_{BE}$ of system bath and environment Hamiltonians $\hat{H}_S$, $\hat{H}_B$, and $\hat{H}_E$ and interaction potentials $\hat{V}_{SB}$ and $\hat{V}_{BE}$. Given such a Hamiltonian, several methods exist to define a unique pointer basis appropriate for the model, summarized in ref 58 and references therein. In principle, this requires only that we are able to write down reasonable models for the system, bath, and environment as separately definable subspaces.

Formally, we can define a system subspace as a Hilbert space upon which all observables that we would like to model act upon. We then partition the remaining degrees of freedom between bath and environment subspaces by requiring that $\hbar \| V_{BE} \| \tau \ll 1$ where $\| A \| = \inf\{c \geq 0: \hat{A}\psi| \leq c|\psi| \ \forall \ \psi \in \mathcal{H}\}$ is the usual operator norm and τ is the time interval that we are interested in modeling. Such definitions are always formally possible and are simply prescribed by the operators and time scales of interest, with longer time scales of interest requiring the explicit inclusion of more degrees of freedom into the bath. In practice, however, this process may require us to include more bath degrees of freedom than can be reasonably simulated, or the model Hamiltonians may be so complicated that the computation of the pointer basis becomes unfeasible. Moreover, in a given setting it may not be obvious which degrees of freedom contribute to a particular experimental observable making the definition of the system difficult.

The resulting distribution can therefore be interpreted as an effective-temperature classical Boltzmann distribution of quantum mechanical minimum uncertainty Gaussian wavepackets taken by scaling the physical temperature, $\beta = \frac{1}{k_B T}$, according to the expression under eq 18. In the low-temperature (or high-frequency) limit the kth mode's effective-temperature approaches 0, and the minimum uncertainty coherent state collapses onto the origin, rendering it equivalent to a harmonic oscillator ground state. In contrast, the high-temperature (or low-frequency) limit of the effective temperature approaches the physical temperature as $T_k' \to T\left(1 - \beta\frac{\hbar\omega_k}{2}\right)$.

4. NUMERICAL RESULTS AND DISCUSSION

In this section, we analyze the heterogeneity of dynamics within a trajectory ensemble of the spin-boson model. We generate this trajectory ensemble following the methodology described in Section 3. To proceed, we substitute eq 18 into eq 14 for the initial Wigner density, interchange the order of integration over coherent state centers and bath phase space initial conditions, and express the time-evolved reduced density matrix as an integral over coherent state centers in the phase space of the bath variables:

$$\sigma(t) \propto \int \mathrm{d}\boldsymbol{P}'\mathrm{d}\boldsymbol{R}' \mathrm{e}^{-\sum_k \beta_k'\left(\frac{1}{2}P_k'^2 + \frac{1}{2}\omega_k^2 R_k'^2\right)} \sigma^{(\boldsymbol{P}',\boldsymbol{R}')}(t) \tag{21}$$

where the matrix elements of $\sigma^{(\boldsymbol{P}',\boldsymbol{R}')}(t)$ involve integrating over the initial conditions sampled around each coherent state center according to eq 14. In our numerical implementation of eq 21, we generate 5000 independent bath coherent state center configurations, $(\boldsymbol{P}', \boldsymbol{R}')$, by Monte Carlo sampling the effective-temperature Boltzmann distribution at a physical temperature of T = 300 K. For each bath configuration, the integrals over phase space initial conditions in eq 14 are computed by averaging over 2×10^4 paths to resolve the initial product of bath minimum uncertainty coherent states and mapping variable coherent states. After averaging over the effective-temperature Boltzmann distribution of single-molecule configurations, one recovers the standard ensemble density matrix description. In every case, the system is initialized in the $|0\rangle\langle 0|$ state. In making a connection with eq 2, we have that the effective-temperature Boltzmann distribution plays the role of the initial distribution function, $P(\Gamma, t = 0)$, while $\sigma^{(\boldsymbol{P}',\boldsymbol{R}')}(t)$ represents the time-revolved single-system density matrix, $\Gamma(t)$. We also emphasize that it is crucial to sum over many semiclassical mapping variable paths to generate each single-system density matrix. Each semiclassical path is not physically meaningful and can display nonphysical properties such as negative populations. Only after summing over many such paths (2×10^4 in these studies) with initial conditions sampled from a wavepacket, in our case a minimum-uncertainty coherent state, can we generate physically meaningful single-system density matrices.

For a two-level spin system, the state space of density operators can be conveniently mapped to the three-dimensional real-valued Bloch sphere. Each single-molecule "trajec-

https://doi.org/10.1021/acs.jctc.1c00477
J. Chem. Theory Comput. 2022, 18, 2047−2061

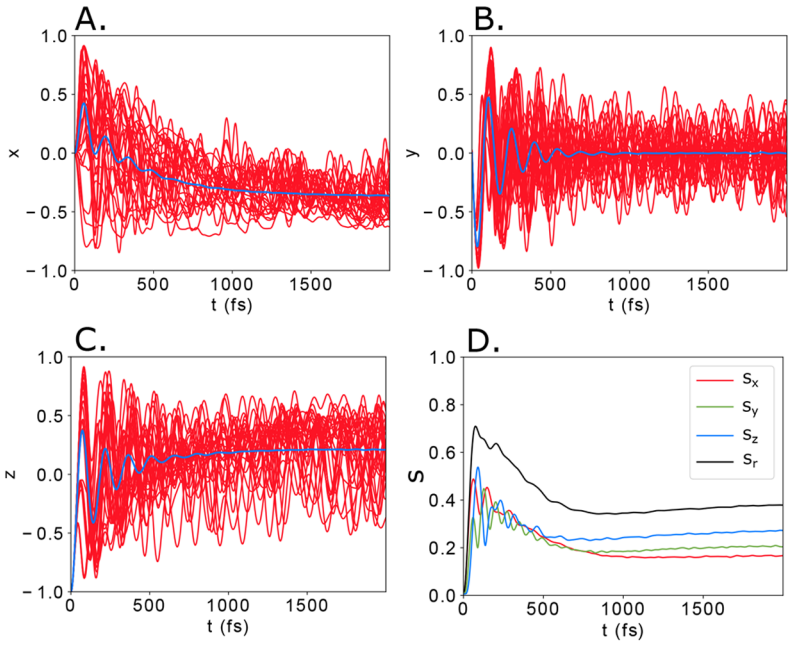

Figure 1. (A–C) Cartesian coordinates of sample single-molecule trajectories (red) and ensemble-averaged trajectory (blue) showing the heterogeneity of dynamics within the ensemble. Each Cartesian coordinate corresponds to the quantum average of the corresponding Pauli spin matrix as defined by eq 22 for an ensemble of trajectories computed using eq 14. (D) Standard deviation of quantum-averaged values for each Pauli matrix within the single-molecule ensemble and for the radial dispersion s_r.

tory", for example, is defined as a time-ordered sequence of points in the Bloch sphere, $\{\sigma(t)\}$, with

$$\sigma(t) = \frac{1}{2}(1 + x(t)S_x + y(t)S_y + z(t)S_z) \tag{22}$$

where x, y, and z are time-dependent real-valued coefficients and $S_x = (|0\rangle\langle 1| + |1\rangle\langle 0|)$, $S_y = i(|0\rangle\langle 1| - |1\rangle\langle 0|)$, and $S_z = (|1\rangle\langle 1| - |0\rangle\langle 0|)$ are the Pauli matrices. We can interpret each Cartesian coordinate $i = \overline{S}_i[\sigma]$ as the quantum average of the Pauli operator S_i for $i = x, y, z$.

This trajectory representation has several useful features. First, the pure state density matrices that indicate the lack of system bath entanglement are found on the surface of the sphere, while states inside the sphere indicate the presence of system bath entanglement. The pure states correspond to the open system states that can be described by a wave function $|\psi\rangle$ with $\rho_{\text{pure}} = |\psi\rangle\langle\psi|$. The z axis describes the relative population of the donor and acceptor sites while the x and y components describe the real and imaginary coherence between the states.

4.1. Heterogeneous Dynamics. Using this coordinate system, the dynamics of individual systems can be visualized and contrasted with the ensemble-averaged dynamics. The x, y, and z components of the trajectory ensemble are plotted in Figure 1. We observe that single-system dynamics differs significantly from one another and from that of the ensemble average. These results highlight the rich distribution of single-molecule dynamics that is obscured by ensemble averaging. Even after 2 ps, where the ensemble-averaged dynamics has relaxed to a steady state, single molecules continue to show significant oscillatory behavior that is washed out when averaged over the ensemble.

The P-ensemble variances given by eq 4c provide a convenient method for quantifying the heterogeneity within these dynamics. The standard deviations in the quantum-averaged spin coordinates $s_i(t) = \sqrt{\text{Var}_P[\overline{S}_i[\sigma(t)]]}$ $(i = x, y, z)$ are defined in eq 4c and can easily be computed from the trajectory ensemble. For any observable A, we simply compute the time-dependent quantum average along each evolving trajectory $\overline{A}[\sigma(t)] = \text{Tr}A\sigma(t)$. The ith trajectory then yields a time series of classical numbers $\overline{A}_i(t)$ that can be analyzed using the usual tools of classical statistics. To obtain the time-dependent standard deviation, we simply use the usual formula for sample standard deviation from classical statistics $s_A(t) = \sqrt{\sum_{i=1}^{N}(\overline{A}_i(t) - \langle\overline{A}(t)\rangle)^2/N}$, where N is the number of trajectories and $\langle\overline{A}(t)\rangle = \sum_{i=1}^{N}\overline{A}_i(t)$ is the sample mean of $\overline{A}_i(t)$. Figure 1D shows the heterogeneity in single-molecule observables within the ensemble. This can be conveniently summarized by the radial dispersion $s_r = \sqrt{s_x^2 + s_y^2 + s_z^2}$ which measures the mean distance of a single-molecule trajectory from the ensemble average.

We find that within the first 100 fs, initially identically prepared single systems rapidly spread around the Bloch sphere before slowly relaxing closer to the ensemble average over time scales of approximately 500 fs due to dissipation and decoherence processes. However, even at 500 fs, the trajectories exhibit significant dispersion from the mean of $s_r \sim 0.4$. Over time scales of 1 ps, the trajectory ensemble slowly broadens, and the influence of the bath leads to a broad, dynamic steady-state distribution.

A more complete picture emerges when the trajectory ensemble is visualized within the Bloch sphere, as plotted in Figure 2. We observe that at early times ~100 fs, trajectories primarily spread out along a ring on the Bloch sphere, defined by rotating the initial state about a precession axis. This indicates that at early times, the primary effect of the bath is to modulate the time scale of the system dynamics without changing its precession axis. Remarkably, at these times, on the

https://doi.org/10.1021/acs.jctc.1c00477
J. Chem. Theory Comput. 2022, 18, 2047–2061

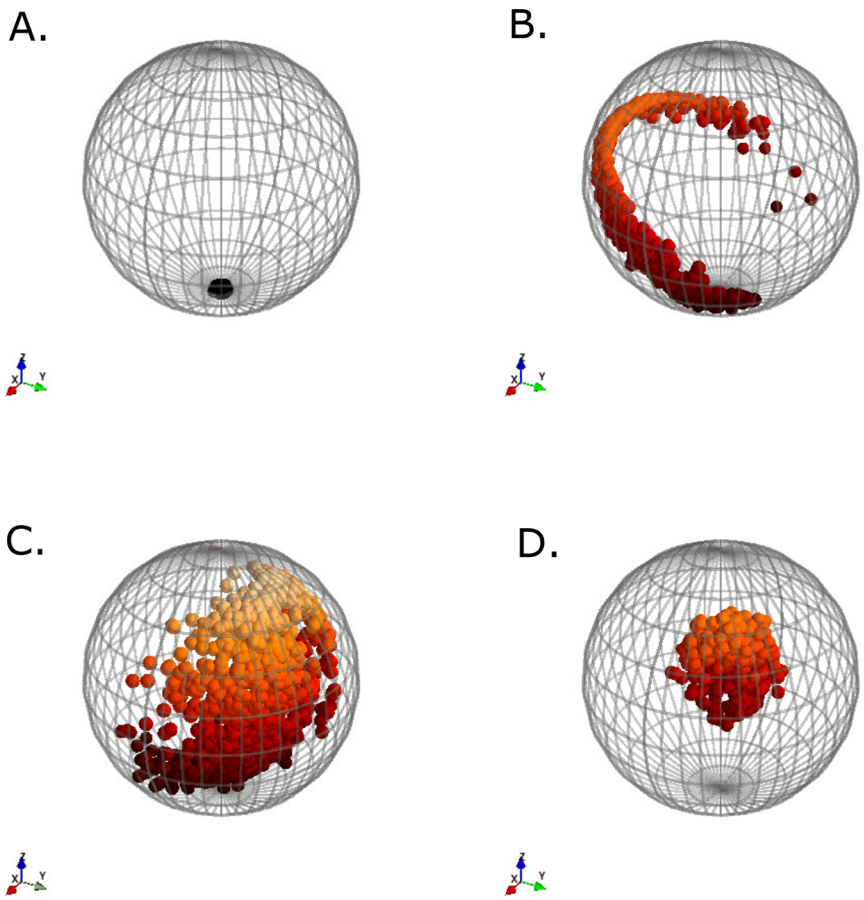

Figure 2. Snapshots of ensemble states at (A) t = 0 fs, (B) t = 100 fs, (C) t = 200 fs, and (D) t = 2 ps (steady state). The color of each point indicates its z coordinate. An ensemble of systems initialized in state $|0\rangle$ fans out along a ring of nearly pure states in the first ∼100 fs. Between 100 and 200 fs the trajectories then spread out around the sphere before dephasing to give a distribution of states inside the Bloch sphere. Notably, most systems do not fully decay to the ensemble-averaged equilibrium leaving a heterogeneous equilibrium distribution.

order of the system-dephasing time, the individual trajectories remain close to the surface of the Bloch sphere, indicating minimal entanglement formation with the bath. This behavior indicates that at early times the influence of the bath on individual systems is dominated by slow modes of the bath that modulate the dynamical frequency of the system, related to $h_{\alpha\beta}(R)$ in eq 12, leading to ensemble coherence loss. This behavior is similar to the frozen mode trajectory approximation, where slow modes of a bosonic bath are stochastically sampled as an intermediate to computing nonmarkovian dynamics.[59]

At intermediate times, ∼200 fs, we observe the tendency for trajectories to spread out over a spherical shell within the Bloch sphere. The diffusion of the trajectories off the ring seen in Figure 2B indicates that the precession axes around which each of the different systems evolve are fluctuating and deviating from one another as faster modes of the bath become involved and modulate the dynamics more significantly. Notably, even at these times, the individual systems remain fairly close to the surface of the unit sphere, indicating that system−bath entanglement is relatively slow to develop with the parameters used in these simulations and that this entanglement is not isotropic about the Bloch sphere, suggesting that some coherence coordinates develop entanglement better than others. In contrast, by ∼2 ps Figure 2D shows the quasi-steady-state distribution of points, indicating a more isotropic distribution around the Bloch sphere that has decayed significantly toward the center of the state. However, even in this quasi-steady state, the distribution retains some width, indicating that even at equilibrium, individual systems behave differently and do not collapse to a maximally entangled state. The width of the sampled distribution is consistent with the prediction of eq 6 that there is a competition between the Shannon entropy of the $P(\Gamma)$, which drives the distribution to broaden, and the entanglement entropy that favors a vanishing Bloch vector radius. Moreover, this partial collapse toward a steady-state distribution of finite width suggests the existence of a fluctuation−dissipation relation to impose balance between heterogeneous interactions with the bath and coherence and energy relaxation processes.

Further insight can be gained by splitting the dynamics into radial and angular components. The dynamical change in the Bloch sphere radius of the trajectories captures the dynamics of entanglement formation between the system and bath and the consequent loss of coherence at the individual system level. By analysis of the statistics of these "radial" dynamics, the mechanism leading to decoherence can be examined to elucidate the dynamics of quantum phase information at the single-system level. In contrast, the angular dynamics at fixed radius captures the complementary dynamical change in quantum phase information as each system coherently evolves under a fluctuating Hamiltonian reflecting the noisy influence

https://doi.org/10.1021/acs.jctc.1c00477
J. Chem. Theory Comput. 2022, 18, 2047−2061

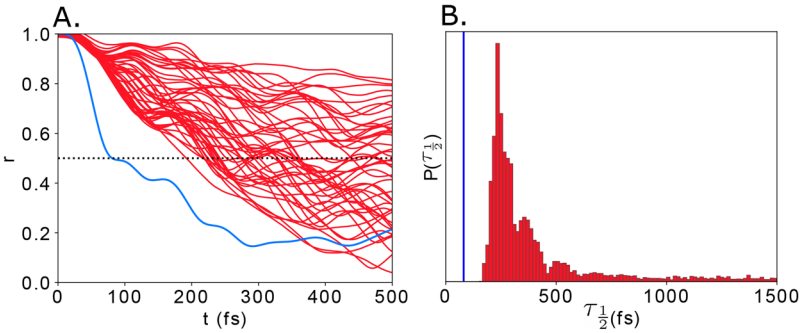

Figure 3. (A) Time-dependent Bloch sphere radii of (red) 50 sample trajectories and (blue) ensemble-averaged density matrices. (B) Histogram of dephasing times, $\tau_{1/2}$, for 5000 trajectories (red) compared to the dephasing time for the ensemble-averaged density matrix (blue). Dephasing times are determined by the first passage time of a trajectory through a sphere with $r_{crit} = \frac{1}{2}$ shown as the dashed line in (A).

of the bath. This "angular" dynamics reveals the dynamical influence of bath interactions on the system dynamics and the role they play in driving heterogeneity in the trajectory ensemble.

4.2. Decoherence and Dephasing. We now consider the heterogeneity in relaxation between different systems in the ensemble. In particular, we are interested in capturing the dephasing mechanisms by which quantum phase information is lost in the ensemble. There are two mechanisms by which phase information is lost. In the first, interaction between the system and bath leads to the formation of entanglement and the loss of quantum phase information to the bath in a process called decoherence. Alternatively, interaction with the bath can lead to fluctuations in the energy levels of the system and therefore in the dynamical frequencies of the system. As a result, different systems in the ensemble evolve with different quantum phases leading to interference and an apparent disappearance of coherence upon ensemble averaging, a process we refer to as heterogeneity-induced dephasing. We note that this accounts for frequency fluctuations at all time scales and therefore includes dephasing due to both static heterogeneity in the Hamiltonians of individual molecules (often referred to as inhomogeneous broadening) and dynamical fluctuations of those Hamiltonians (often referred to as homogeneous broadening).

By monitoring the coherence of the systems at the trajectory level, we are able to resolve these two process separately. To do this, we note that the coherence of a quantum state can be captured by its purity

$$\mathrm{Pur}(\rho) = \mathrm{Tr}\rho^2 = \frac{1}{4}(1 + x^2 + y^2 + z^2) = \frac{1}{4}(1 + r^2) \tag{23}$$

which is related to its Bloch sphere radius, r. The purity quantifies the entanglement between the system and the bath with $\mathrm{Pur}(\rho) = 1$ indicating a pure state with no system bath entanglement and $\mathrm{Pur}(\rho) \to \frac{1}{4}$ indicating a maximally entangled state.

Therefore, by analyzing the radial dynamics of individual trajectories we can not only determine the relative contribution of heterogeneity-induced dephasing and decoherence mechanisms but also examine the heterogeneity in decoherence time scales within the ensemble. By plotting these radial trajectories alongside the ensemble-averaged dynamics, as shown in Figure 3A, we find that individual systems dephase much slower than the ensemble-averaged trajectory. In particular, at time scales on the order of ∼100−200 fs, we see that the ensemble-averaged trajectory (blue trace) rapidly dephases, leading to a decrease in its radius. In contrast, nearly all of the individual trajectories (red traces) retain a much higher purity $r > 0.5$ at these time scales, indicating that heterogeneity-induced dephasing rather than system−bath entanglement is responsible for the early time dephasing of the ensemble average. In the context of our spin-boson system, this result is consistent with the primarily transverse diffusion of trajectories onto rings and hollow spherical shells in Figure 2B and C. The opposite case where dephasing is dominated by entanglement phase loss would show most of the single-system trajectories decreasing in radius at approximately the same time scale as the ensemble-averaged trajectory.

This finding is not without precedent, as a similar observation has been made in the modeling of photosynthetic light-harvesting systems,[60] line widths in single-molecule spectroscopy,[61,62] as well as coherent single-molecule experiments.[14−17] In these studies, single molecules are seen to have narrower spectral line widths than the ensemble, leading to a distinction between inhomogeneous broadening (present only in the ensemble spectrum) due to static heterogeneity between the transition frequencies of individual molecules and homogeneous broadening due to unresolved dynamic fluctuations in the transition frequency of each molecule during the measurement. Since both of these mechanisms lead to dephasing, the longer lifetimes of the single molecules compared to the ensemble are then attributed to the lack of inhomogeneous broadening in the single-molecule spectrum. While the results we present appear qualitatively similar, the physical mechanism behind the longer coherence time of single molecules is very different. In the trajectory ensemble, both the static and dynamic variabilities in the transition frequency are captured by the single-molecule trajectories. Both of these dephasing sources, which correspond to the same physical mechanism and differ only in how they are *resolved* in a given experiment, are treated as heterogeneity-induced dephasing and do not play a role in the coherence loss of the single-molecule trajectories. They both lead to fluctuations in the angular dynamics at a fixed radius that we will consider at length in the following section. This single-molecule coherence loss in our simulations arises only due to the formation of entanglement between the system and bath (i.e., true decoherence). The rich dynamics and distribution of single-molecule decoherence behavior we see in Figure 3 describe only this dynamic entanglement formation between the system

https://doi.org/10.1021/acs.jctc.1c00477
J. Chem. Theory Comput. 2022, 18, 2047−2061

and bath. As we discussed in Section 3.2, the trajectory ensemble we study here corresponds to the limit where the maximum allowable information about the bath configuration has been obtained. These decoherence time statistics therefore capture the longest possible coherence times that can be achieved by accounting for all bath-induced frequency fluctuations.

Analysis of the histogram plotted in Figure 3B reveals that the individual systems show significant heterogeneity in their decoherence time scales. Evidently, certain initial bath states entangle with the system much more slowly than others, leading the system to retain quantum phase information for longer times. By understanding the entanglement process at the single-system level, it may be possible to design systems that promote the well-insulated bath states to protect coherence in the system. This radial dynamics exhibits highly nonexponential decay, making the quantification of decoherence times difficult. We therefore define the decoherence time, $\tau_{1/2}$, as the time of first passage through a shell within the Bloch sphere of radius $r = \frac{1}{2}$.

The distribution of $\tau_{1/2}$ values is plotted in Figure 3B. We observe significant heterogeneity in this measure of decoherence time with a distributional mean and standard deviation of 447 and 371 fs, respectively. The distribution of decoherence times is asymmetric with a fat tail at larger values of $\tau_{1/2}$, corresponding to a subpopulation of systems that are especially slow to develop entanglement. Approximately 12% of all single-molecule trajectories fail to cross the cutoff radius of $r = \frac{1}{2}$ during their 2 ps trajectory, indicating the existence of bath states that allow the system to retain most of its quantum phase information.

As shown in Figure 3A, at the single-system level we observe significant oscillations in r rather than the mostly monotonic decay seen in the ensemble average, indicating that phase information does not flow unidirectionally from the system to the bath, as one would conclude based on the ensemble-averaged behavior. Similarly, the rapid decrease in r observed in the ensemble behavior cannot be reliably interpreted to quantify system−bath entanglement or ensemble dephasing because it convolutes these two effects. The oscillations in r for single-system dynamics indicate that system phase information can delocalize into the bath and return to the system, driven by certain modes of the system−bath interaction. In fact, this fluctuating radial dynamics is the mechanism behind the broad steady-state distribution and balances the entanglement-driven relaxation to prevent total collapse onto the maximum entropy state.

4.3. Heterogeneity in System Dynamics. We now turn our attention to the angular dynamics within spherical shells of fixed radii. This dynamics predominantly captures the coherent evolution of the spin system under the influence of the fluctuating bath. The angular dynamics effectively projects out the incoherent relaxation processes considered in the previous section, which act in the longitudinal direction. A convenient way to visualize the angular dynamics is to plot the precession axis implied by the system dynamics. Since the unitary coherent dynamics of spin systems precesses about an axis defined by an effective Hamiltonian in Bloch sphere coordinates, the dynamical change in the direction and magnitude of the axis captures the influence of the fluctuating bath. The rotation axis is equivalent to the angular velocity studied in classical Langevin analysis of the rotational diffusion of rigid bodies.

To extract the axis of rotation from the dynamical trajectory, we apply Rodrigues' rotation formula for the rotation axis $\boldsymbol{\xi}$ between two points $\boldsymbol{a}$ and $\boldsymbol{b}$

$$\tilde{\boldsymbol{\xi}} = \frac{\boldsymbol{a} \times \boldsymbol{b}}{|\boldsymbol{a} \times \boldsymbol{b}|} \tag{24a}$$

$$\cos(|\boldsymbol{\xi}|) = \frac{\mathbf{a} \cdot \mathbf{b}}{|a||b|} \tag{24b}$$

where the first expression gives the unit vector $\tilde{\boldsymbol{\xi}}$ of rotation, and its norm, under the Euler vector convention, is given in the second expression by the angle of rotation. Letting $\boldsymbol{a} = \boldsymbol{\rho}(t)$ (the Bloch vector at time t) and $\boldsymbol{b} = \boldsymbol{\rho}(t + \delta t)$ be two adjacent time steps in the trajectory and assuming negligible dephasing in one time step of $\delta t = 1$ fs, we can rewrite these equations to give

$$\tilde{\boldsymbol{\xi}} = \frac{\boldsymbol{\rho} \times \dot{\boldsymbol{\rho}}}{|\boldsymbol{\rho} \times \dot{\boldsymbol{\rho}}|} \tag{25a}$$

$$\cos(|\boldsymbol{\xi}|) \approx 1 + \frac{\boldsymbol{\rho} \cdot \dot{\boldsymbol{\rho}}}{|\rho|^2} \delta t \tag{25b}$$

Taking the small-angle approximation, valid for small δt, we obtain the approximate expression $|\xi| \approx \rho \cdot \dot{\rho} \delta t / |\rho|2$. In Figure 4,

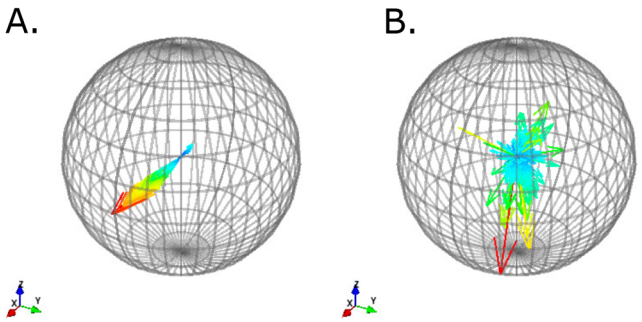

Figure 4. Distribution of precession axes $\boldsymbol{\xi}$ represented by their Euler vectors, defined in eq 25a at (A) $t = 0$ fs and (B) $t = 2$ ps in the steady state. These axes represent the system Hamiltonian and the fluctuating random force that arises due to bath dynamics. The color of each vector shows its magnitude.

we plot these precession axes at the initial, $t = 0$ ps, and final, $t = 2$ ps, simulation time steps. This plot shows that, at early times, individual trajectories precess along the same axis but at different frequencies. This behavior corresponds to the early time spread of trajectories around a ring defined by the precession axis as seen in Figure 2B. At later times, however, the direction of the axes has randomized, indicating that different trajectories precess in different directions, spreading out around the sphere as seen in Figure 2C and D.

Following the procedure used in classical Langevin analysis, we systematically study the effect of bath fluctuations by considering the axis−axis correlation function

$$C_{\xi\xi}(s, t) = \langle \boldsymbol{\xi}(s) \cdot \boldsymbol{\xi}(t) \rangle - \langle \boldsymbol{\xi}(s) \rangle \langle \boldsymbol{\xi}(t) \rangle \tag{26}$$

where $\langle \cdot \rangle$ denotes the average over the P-ensemble distribution as in eq 2, which can be equivalently computed by averaging over the trajectory ensemble. At equilibrium, where the start time $s \to -\infty$, this expression is invariant under time

https://doi.org/10.1021/acs.jctc.1c00477
J. Chem. Theory Comput. 2022, 18, 2047−2061

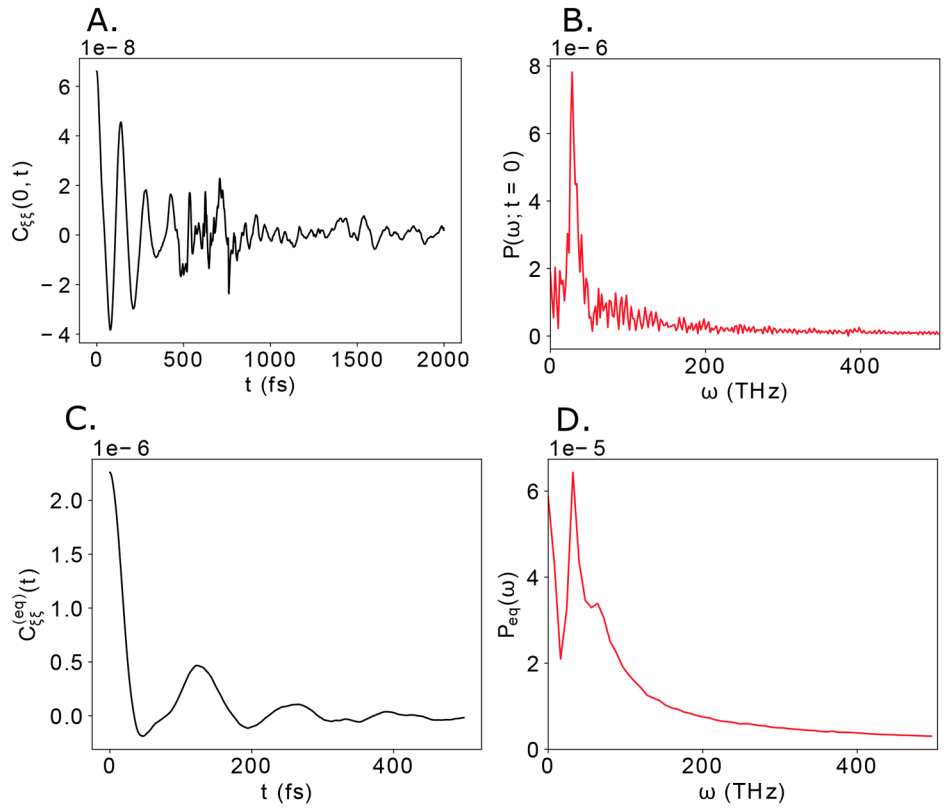

Figure 5. Axis−axis correlation functions starting at (A) $t = 0$ fs and (C) at equilibrium $t \geq 1$ ps. Correlation functions were computed using $n = 5000$ trajectories of length $\tau = 2$ ps, sampled every $\Delta t = 1$ fs. The power spectra from $t = 0$ and at equilibrium are shown in (B) and (D), respectively. At both times, axis fluctuations show the signatures of bath oscillations at a frequency of $\omega \approx 36$ THz.

translation and therefore only depends on $\tau = t - s$ giving the one index notation $C^{(eq)}_{\xi\xi}(t)$.

By plotting both of these time correlation functions in Figure 5, we see that the axis fluctuations indicate the presence of marked oscillations on the tens of femtoseconds time scale. These time scales can be systematically analyzed by considering the power spectrum of these fluctuations, obtained by taking the magnitude of the Fourier transform of $C_{\xi\xi}$. The resulting frequency domain analysis shows a clear peak at ∼40 THz, corresponding to 2γ, where γ is the frequency peak of the Drude−Lorentz spectral density that characterizes the boson bath. In this model, we considered a simple parametrized bath model that allows us to directly compare the observed power spectrum to the bath density of states. However, in more complicated settings, the spectral properties of the nuclear bath are often unknown. By analyzing the dynamical correlation functions of single-system dynamics, we see that they can provide powerful tools for directly extracting the statistical and dynamical properties of the relevant bath fluctuations.

4.4. Entanglement Entropy. System−bath entanglement plays a significant role in determining $P(\Gamma)$ at longer times. As we observe in Figures 2 and 3, as the ensemble approaches steady state, ∼500 fs, the systems occupy a region of the Bloch sphere with a range of r-values around $\langle r[\Gamma]\rangle \approx 0.1-0.8$ that can be significantly larger than that of the ensemble density matrix, $r[\rho] \approx 0.2$. Because the single-system states are not influenced by heterogeneity-induced dephasing, their values of r report directly on their level of entanglement with the bath. Thus, $P(\Gamma)$ encodes the statistics necessary to quantify the thermodynamic influence of system−bath entanglement.

The specific distribution of Bloch sphere coordinates that emerge at larger times reflects a balance between competing entropic factors. The distributional entropy of the system is maximized when $r = 1$, thus favoring states along the surface of the Bloch sphere. On the other hand, system−bath entanglement favors states with $r = 0$. The steady-state distribution of $P(\Gamma)$ reflects the thermodynamic balance between these two effects.

The thermodynamic considerations outlined in eq 6 show that the same mathematical trade-off arises between the Shannon entropy of the distribution used in the entropy maximization process and the free energy $\bar{H} - TS_e$. The first contribution in this state-space free energy is easily understood as the quantum average energy of a given state, describing the energetic bias toward lower energy states of the spin system. The physical interpretation of the entanglement entropy as well as its mathematical computation is more challenging. As discussed in Section 2.2 the entanglement entropy describes the entropic drive toward forming system−bath entanglement, since there are many more entangled system−bath states than pure ones in the composite state space. As such, it can be understood as the entropic bias of the collective coordinate defined by the system-reduced density matrix σ. This opens up a variety of tools from classical statistical mechanics for the free energetic analysis and potential biasing of collective coordinates.

Here we have considered the simplest problem of free energy estimation from a trajectory ensemble. We begin by estimating the probability distribution by collecting all time points $t > 1.5$ ps in the trajectory ensemble. We proceed by

https://doi.org/10.1021/acs.jctc.1c00477
J. Chem. Theory Comput. 2022, 18, 2047−2061

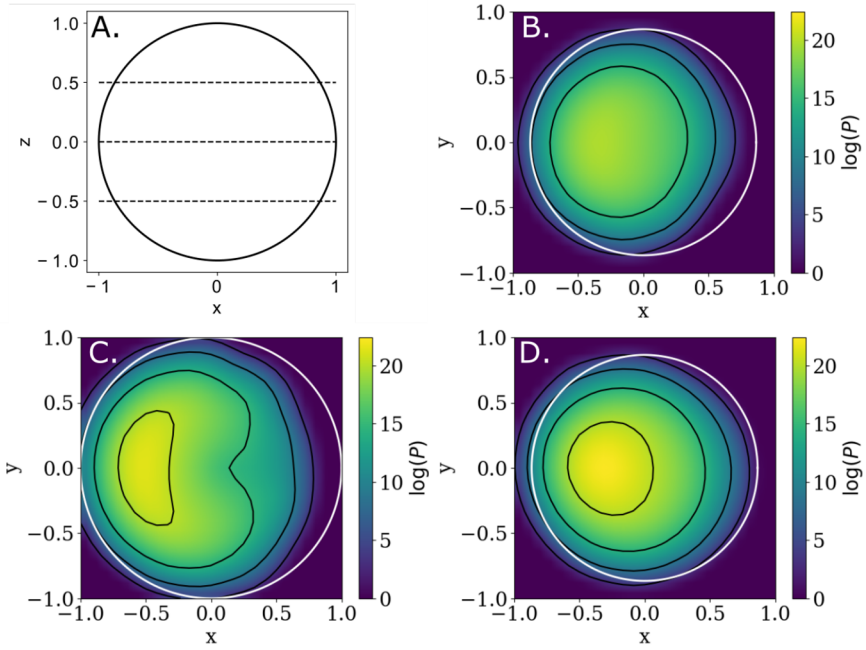

Figure 6. Free energy estimates $\log(P)$ are shown at three slices through the Bloch sphere indicated in (A) at (B) $z = -1/2$, (C) $z = 0$, and (D) $z = 1/2$. The probability density $P(\sigma)$ was computed using a Gaussian kernel density estimate with Scott's rule used in bandwidth selection. Black contours indicate the distribution at $\log(P) = 5$, 10, 15, and 20. The distribution was estimated using all time steps after $t \geq 1.5$ ps. The system has not fully equilibrated in these simulations but nevertheless shows that even at long times, where the ensemble-averaged density matrix ρ has reached equilibrium, the single-molecule distribution does not fully collapse onto the ensemble-averaged equilibrium state.

performing a Gaussian density estimation using this discrete sampling from the near-equilibrium distribution using Scott's rule for bandwidth selection. This procedure places a Gaussian distribution at each sampled point and sums over the ensemble to obtain an estimated continuous probability density. Once the distribution has been obtained, the free energy can be easily calculated as $F(\sigma) = -k_B T \ln(P(\sigma))$ and is plotted in Figure 6.

The inhomogeneity we observe in these results indicates that the system has not fully equilibrated. The initial system distribution, a δ function at the south pole of the Bloch sphere, is very far from equilibrium and could not be equilibrated on the simulation time scale. This observation is surprising since the ensemble dynamics equilibrated on a time scale ~500 fs while the single-molecule distribution still shows signatures of the initial state ~2 ps. These results indicate that single-molecule distributions can display interesting dynamics long after the ensemble-average has reached its steady state.

5. CONCLUSION

In this paper, we have presented an efficient method for sampling and simulating the quantum dynamics underlying coherent single-molecule experiments and applied it to the canonical example of a spin-boson model. We then exploited the geometric isomorphism between classical phase space and Liouville space under the state-space distribution formalism to analyze the resulting trajectory ensemble using an approach analogous to classical statistical mechanics. These analyses have revealed a remarkable heterogeneity in the decoherence properties within single-molecule ensembles and showed that even at room temperature, a significant proportion, ~12%, of single molecules within an ensemble may retain substantial coherence even when the ensemble has fully decohered. This result motivates future systematic study of the bath states responsible for these long-lived coherences in order to drive the design of systems with long-lived coherent dynamics at room temperature through bath engineering. Moreover, we showed that the statistics of bath fluctuations that drive the heterogeneity between single molecules can be extracted and reflect the underlying bath density of states, providing new tools for the analysis of quantum dynamical trajectories.

By showing that the reduced density matrix of the system is a collective coordinate of the overall system−bath state, we have also used the trajectory ensemble to compute a thermodynamic entanglement entropy that quantifies the thermodynamic drive toward entanglement in open quantum systems. Taken together, these results present a practical set of tools for simulating and analyzing the results of single-molecule experiments and highlight the insight that can be gained from the thermodynamic analysis of these ensembles. For example, similar analysis can be applied to gain single-molecule insight into recent studies that used quantum classical trajectories to compute ensemble-averaged full counting statistics of currents in molecular junctions.[63,64]

AUTHOR INFORMATION

Corresponding Authors

Adam P. Willard − *Department of Chemistry, Massachusetts Institute of Technology, Cambridge, Massachusetts 02139, United States;* orcid.org/0000-0002-0934-4737; Email: awillard@mit.edu

David F. Coker − *Department of Chemistry, Boston University, Boston, Massachusetts 02215, United States;* orcid.org/0000-0001-6210-5228; Email: coker@bu.edu

https://doi.org/10.1021/acs.jctc.1c00477
J. Chem. Theory Comput. 2022, 18, 2047−2061

Authors

Amro Dodin − *Department of Chemistry, Massachusetts Institute of Technology, Cambridge, Massachusetts 02139, United States*

Justin Provazza − *Department of Chemistry, Northwestern University, Evanston, Illinois 60208, United States; Department of Chemistry, Boston University, Boston, Massachusetts 02215, United States*

Complete contact information is available at: https://pubs.acs.org/10.1021/acs.jctc.1c00477

Author Contributions

†A.D. and J.P. are co-first authors and contributed equally to this work.

Notes

The authors declare no competing financial interest.

■ ACKNOWLEDGMENTS

D.F.C. and J.P. acknowledge support for this research from the U.S. Department of Energy, Office of Basic Energy Sciences under contract DE-SC0020437 and from the National Science Foundation under grant CHE-1955 407. A.P.W. and A.D. acknowledge support for this research from the U.S. Department of Energy (DOE), Office of Science, Basic Energy Sciences under Award DE-SC0019998.

■ REFERENCES

(1) Moerner, W. E. A Dozen Years of Single-Molecule Spectroscopy in Physics, Chemistry, and Biophysics. *J. Phys. Chem. B* **2002**, *106*, 910.

(2) Moerner, W. E. Nobel Lecture: Single-molecule spectroscopy, imaging, and photocontrol: Foundations for super-resolution microscopy. *Rev. Mod. Phys.* **2015**, *87*, 1183−1212.

(3) Tamarat, P.; Maali, A.; Lounis, B.; Orrit, M. Ten Years of Single-Molecule Spectroscopy. *J. Phys. Chem. A* **2000**, *104*, 1−16.

(4) Nirmal, M.; Dabbousi, B. O.; Bawendi, M. G.; Macklin, J. J.; Trautman, J. K.; Harris, T. D.; Brus, L. E. Fluorescence intermittency in single cadmium selenide nanocrystals. *Nature* **1996**, *383*, 802−804.

(5) Yildiz, A.; Forkey, J. N.; McKinney, S. A.; Ha, T.; Goldman, Y. E.; Selvin, P. R. Myosin V Walks Hand-Over-Hand: Single Fluorophore Imaging with 1.5-nm Localization. *Science* **2003**, *300*, 2061−2065.

(6) Kondo, T.; Pinnola, A.; Chen, W. J.; Dall'Osto, L.; Bassi, R.; Schlau-Cohen, G. S. Single-molecule spectroscopy of LHCSR1 protein dynamics identifies two distinct states responsible for multi-timescale photosynthetic photoprotection. *Nat. Chem.* **2017**, *9*, 772−778.

(7) Mukamel, S. *Principles of Nonlinear Optical Spectroscopy*; Oxford University Press: New York, 1999.

(8) Fleming, G. R.; Schlau-Cohen, G. S.; Amarnath, K.; Zaks, J. Design principles of photosynthetic light-harvesting. *Faraday Discuss.* **2012**, *155*, 27−41.

(9) Cheng, Y.-C.; Fleming, G. R. Dynamics of Light Harvesting in Photosynthesis. *Annu. Rev. Phys. Chem.* **2009**, *60*, 241−262.

(10) Engel, G. S.; Calhoun, T. R.; Read, E. L.; Ahn, T.-K.; Mančal, T.; Cheng, Y.-C.; Blankenship, R. E.; Fleming, G. R. Evidence for wavelike energy transfer through quantum coherence in photosynthetic systems. *Nature (London)* **2007**, *446*, 782−786.

(11) Collini, E.; Wong, C. Y.; Wilk, K. E.; Curmi, P. M. G.; Brumer, P.; Scholes, G. D. Coherently wired light-harvesting in photosynthetic marine algae at ambient temperature. *Nature (London)* **2010**, *463*, 644−647.

(12) Chenu, A.; Scholes, G. D. Coherence in Energy Transfer and Photosynthesis. *Annu. Rev. Phys. Chem.* **2015**, *66*, 69−96.

(13) Johnson, P. J. M.; Halpin, A.; Morizumi, T.; Prokhorenko, V. I.; Ernst, O. P.; Miller, R. J. D. Local vibrational coherences drive the primary photochemistry of vision. *Nat. Chem.* **2015**, *7*, 980−986.

(14) Brinks, D.; Hildner, R.; van Dijk, E. M. H. P.; Stefani, F. D.; Nieder, J. B.; Hernando, J.; van Hulst, N. F. Ultrafast dynamics of single molecules. *Chem. Soc. Rev.* **2014**, *43*, 2476−2491.

(15) Hildner, R.; Brinks, D.; Nieder, J. B.; Cogdell, R. J.; van Hulst, N. F. Quantum Coherent Energy Transfer over Varying Pathways in Single Light-Harvesting Complexes. *Science* **2013**, *340*, 1448−1451.

(16) Hildner, R.; Brinks, D.; van Hulst, N. F. Femtosecond coherence and quantum control of single molecules at room temperature. *Nat. Phys.* **2011**, *7*, 172−177.

(17) Brinks, D.; Stefani, F. D.; Kulzer, F.; Hildner, R.; Taminiau, T. H.; Avlasevich, Y.; Müllen, K.; van Hulst, N. F. Visualizing and controlling vibrational wave packets of single molecules. *Nature* **2010**, *465*, 905−908.

(18) Shapiro, M.; Brumer, P. *Quantum Control of Molecular Processes*, 2nd ed.; Wiley-VCH: Weinheim, Germany, 2012.

(19) Bernardi, R. C.; Melo, M. C. R.; Schulten, K. Enhanced sampling techniques in molecular dynamics simulations of biological systems. *Biochimica et Biophysica Acta (BBA)-General Subjects* **2015**, *1850*, 872−877.

(20) Abrams, C.; Bussi, G. Enhanced Sampling in Molecular Dynamics Using Metadynamics, Replica-Exchange, and Temperature-Acceleration. *Entropy* **2014**, *16*, 163−199.

(21) Jarzynski, C. Equalities and Inequalities: Irreversibility and the Second Law of Thermodynamics at the Nanoscale. *Annual Review of Condensed Matter Physics* **2011**, *2*, 329−351.

(22) Campisi, M.; Hänggi, P.; Talkner, P. Colloquium: Quantum fluctuation relations: Foundations and applications. *Rev. Mod. Phys.* **2011**, *83*, 771−791.

(23) Seifert, U. Stochastic thermodynamics: principles and perspectives. *Eur. Phys. J. B* **2008**, *64*, 423−431.

(24) Esposito, M.; Mukamel, S. Fluctuation theorems for quantum master equations. *Phys. Rev. E* **2006**, *73*, 046129.

(25) Evans, D. J.; Searles, D. J. The Fluctuation Theorem. *Adv. Phys.* **2002**, *51*, 1529−1585.

(26) Dodin, A.; Willard, A. P. State space distribution and dynamical flow for closed and open quantum systems. *J. Chem. Phys.* **2019**, *151*, 064106.

(27) Blum, K. *Density Matrix Theory and Applications*; Springer Science & Business Media: Berlin/Heidelberg, Germany, 2012.

(28) Breuer, H.-P.; Petruccione, F. *The Theory of Open Quantum Systems*; Oxford University Press: Oxford, U.K., 2007.

(29) Davies, E. B. Quantum stochastic processes. *Comm. Math. Phys.* **1969**, *15*, 277−304.

(30) Plenio, M. B.; Knight, P. L. The quantum-jump approach to dissipative dynamics in quantum optics. *Rev. Mod. Phys.* **1998**, *70*, 101−144.

(31) Percival, I. *Quantum State Diffusion*; Cambridge University Press: Cambridge, U.K., 1998.

(32) Gisin, N.; Percival, I. C. The quantum-state diffusion model applied to open systems. *J. Phys. A Math. Gen.* **1992**, *25*, 5677−567.

(33) Dum, R.; Zoller, P.; Ritsch, H. Monte Carlo simulation of the atomic master equation for spontaneous emission. *Phys. Rev. A* **1992**, *45*, 4879−4887.

(34) Dong, D.; Petersen, I. R. Quantum control theory and applications: a survey. *IET Control Theory & Applications* **2010**, *4*, 2651−2671.

(35) Wiseman, H. M.; Milburn, G. J. *Quantum Measurement and Control*; Cambridge University Press: Cambridge, U.K., 2009.

(36) Wiseman, H. M.; Milburn, G. J. Interpretation of quantum jump and diffusion processes illustrated on the Bloch sphere. *Phys. Rev. A* **1993**, *47*, 1652−1666.

(37) Barchielli, A.; Belavkin, V. P. Measurements continuous in time and a posteriori states in quantum mechanics. *J. Phys. A: Math. Gen.* **1991**, *24*, 1495.

(38) Jaynes, E. T. Information Theory and Statistical Mechanics. *Phys. Rev.* **1957**, *106*, 620−630.

(39) Jaynes, E. T. Information Theory and Statistical Mechanics. II. *Phys. Rev.* **1957**, *108*, 171−190.
(40) Jaynes, E. T. Monkeys, Kangaroos, and N. In *Maximum-Entropy and Bayesian Methods in Applied Statistics*; Justice, J. H., Ed.; Cambridge University Press: Cambridge, U.K., 1986; p 26.
(41) Jarzynski, C. Nonequilibrium work theorem for a system strongly coupled to a thermal environment. *J. Stat. Mech.* **2004**, *2004*, P09005.
(42) Meyer, H.-D.; Miller, W. H. A classical analog for electronic degrees of freedom in nonadiabatic collision processes. *J. Chem. Phys.* **1979**, *70*, 3214.
(43) Stock, G.; Thoss, M. Semiclassical Description of Nonadiabatic Quantum Dynamics. *Phys. Rev. Lett.* **1997**, *78*, 578−581.
(44) Thoss, M.; Stock, G. Mapping Approach to the Semiclassical Description of Nonadiabatic Quantum Dynamics. *Phys. Rev. A* **1999**, *59*, 64.
(45) Wang, H.; Song, X.; Chandler, D.; Miller, W. H. Semiclassical study of electronically nonadiabatic dynamics in the condensed-phase: Spin-boson problem with Debye spectral density. *J. Chem. Phys.* **1999**, *110*, 4828−4840.
(46) Huo, P.; Coker, D. F. Communication: Partial linearized density matrix dynamics for dissipative, non-adiabatic quantum evolution. *J. Chem. Phys.* **2011**, *135*, 201101.
(47) Polkovnikov, A. Phase space representation of quantum dynamics. *Annals of Physics* **2010**, *325*, 1790−1852.
(48) Lee, M. K.; Huo, P.; Coker, D. F. Semiclassical Path Integral Dynamics: Photosynthetic Energy Transfer with Realistic Environment Interactions. *Annu. Rev. Phys. Chem.* **2016**, *67*, 639−668.
(49) Provazza, J.; Segatta, F.; Garavelli, M.; Coker, D. F. Semiclassical Path Integral Calculation of Nonlinear Optical Spectroscopy. *J. Chem. Theory Comput.* **2018**, *14*, 856−866.
(50) Huo, P.; Miller, T.; Coker, D. Communication: Predictive partial linearized path integral simulation of condensed phase electron transfer dynamics. *J. Chem. Phys.* **2013**, *139*, 151103.
(51) Mandal, A.; Huo, P. Investigating New Reactivities Enabled by Polariton Photochemistry. *J. Phys. Chem. Lett.* **2019**, *10*, 5519−5529.
(52) Provazza, J.; Tempelaar, R.; Coker, D. F. Analytic and numerical vibronic spectra from quasi-classical trajectory ensembles. *J. Chem. Phys.* **2021**, *155*, 014108.
(53) Bonella, S.; Coker, D. F. LAND-map, a linearized approach to nonadiabatic dynamics using the mapping formalism. *J. Chem. Phys.* **2005**, *122*, 194102.
(54) Provazza, J.; Segatta, F.; Coker, D. F. Modeling non-perturbative field-driven vibronic dynamics: Selective state preparation and non-linear spectroscopy. *J. Chem. Theory Comput.* **2021**, *17*, 29−39.
(55) Kübler, O.; Zeh, H. D. Dynamics of quantum correlations. *Annals of Physics* **1973**, *76*, 405−418.
(56) Zurek, W. H. Pointer basis of quantum apparatus: Into what mixture does the wave packet collapse? *Phys. Rev. D* **1981**, *24*, 1516−1525.
(57) Zurek, W. H.; Habib, S.; Paz, J. P. Coherent states via decoherence. *Phys. Rev. Lett.* **1993**, *70*, 1187−1190.
(58) Schlosshauer, M. A. Decoherence and the Quantum-To-Classical Transition. *The Frontiers Collection*; Springer-Verlag: Berlin/Heidelberg, Germany, 2007.
(59) Montoya-Castillo, A.; Berkelbach, T. C.; Reichman, D. R. Extending the applicability of Redfield theories into highly non-Markovian regimes. *J. Chem. Phys.* **2015**, *143*, 194108.
(60) Ishizaki, A.; Fleming, G. R. On the Interpretation of Quantum Coherent Beats Observed in Two-Dimensional Electronic Spectra of Photosynthetic Light Harvesting Complexes. *J. Phys. Chem. B* **2011**, *115*, 6227−6233.
(61) Geva, E.; Skinner, J. L. Theory of Single-Molecule Optical Line-Shape Distributions in Low-Temperature Glasses. *J. Phys. Chem. B* **1997**, *101*, 8920−8932.
(62) Ka, B. J.; Zhang, M.-L.; Geva, E. Homogeneity and Markovity of electronic dephasing in liquid solutions. *J. Chem. Phys.* **2006**, *125*, 124509.
(63) Liu, J.; Hsieh, C.-Y.; Segal, D.; Hanna, G. Heat transfer statistics in mixed quantum-classical systems. *J. Chem. Phys.* **2018**, *149*, 224104.
(64) Liu, J.; Segal, D.; Hanna, G. Hybrid quantum-classical simulation of quantum speed limits in open quantum systems. *J. Phys. A: Math. Theor.* **2019**, *52*, 215301.

https://doi.org/10.1021/acs.jctc.1c00477
J. Chem. Theory Comput. 2022, 18, 2047−2061